# How to Print High-Mobility Metal Oxide Transistors – Recent Advances in Ink Design, Processing, and Device Engineering

*William J. Scheideler[1] and Vivek Subramanian*[*,2]*

W.J. Scheideler
Thayer School of Engineering
Dartmouth College, Hanover, NH 03755, United States

V. Subramanian
Institute of Electrical and Microengineering,
École polytechnique fédérale de Lausanne,
Lausanne, Switzerland
E-mail: vivek.subramanian@epfl.ch

Keywords: *printed metal oxides, thin film transistors, amorphous oxide semiconductors, transparent electronics*

**Abstract**

High-throughput printing-based fabrication has emerged as a key enabler of flexible electronics given its unique capability for low-cost integration of circuits based on printed thin film transistors (TFTs). Research in printing inorganic metal oxides has revealed the potential for fabricating oxide TFTs with an unmatched combination of high electron mobility and optical transparency. Here, we highlight recent developments in ink chemistry, printing physics, and material design for high-mobility metal oxide transistors. We consider ongoing challenges for this field include lowering process temperatures, achieving high speed and high resolution printing, and balancing device performance with the need for high mechanical flexibility. Finally, we provide a roadmap for overcoming these challenges with emerging synthetic strategies for fabricating 2D oxides and complementary TFT circuits for flexible electronics.

## 1. Introduction

Flexible electronics has intrinsic potential to alter the paradigms of cost, weight, form factor, and sustainability limiting large-area devices such as displays, sensors, and wearables. High-throughput printing-based fabrication could become a key technology enabling emerging flexible electronics given that it offers digital on-demand manufacturing[1], diverse integration of nanomaterials with advanced properties for energy storage[2], biomedical sensing[3], and display[4], and the potential for low-cost fabrication of circuits based on printed transistors[5]. Towards this goal of printing active devices, transparent metal oxides offer superlative electronic performance[6] amongst other printed semiconductors, even considering recent advances in organic semiconductors and 2D chalcogenides. The combination of high mobility and low processing temperatures that has propelled the commercialization of oxides in displays[7] provides an opportunity to fabricate high performance flexible electronics with 100 MHz-class operating frequencies[8].

Metal oxides are a powerful material set for optoelectronics because they offer high visible range transparency as well as wide or ultrawide bandgaps, which make them useful for high-mobility semiconductors ($\mu_{eff}$ > 10 $cm^2/Vs$) and conductive electrodes ($\sigma$ > 1000 S/cm) as well as high-k dielectrics. The synthetic simplicity of metal oxides also provides cost advantages over competing printed transistor materials (carbon nanotubes, organic semiconductors, etc.). Metal oxides are processed from abundant, inexpensive[9] metal salts, an essential characteristic for displacing incumbent vacuum technologies such as sputtering. However, leveraging this synthetic route requires careful ink design balancing the physics of printing with the chemistry of film conversion – a complex process involving precursor decomposition and volatilization as well as densification and crystallization into the solid oxide.

Here, we provide a perspective highlighting metal oxide ink design for printing high-mobility transistors at low temperatures. We first consider the impact of ink formulation on the physics of printing and describe the dominant phenomena governing film formation and device integration (Figure 1a). We then discuss recent advances in fully printed devices consisting of metal oxide electrodes, semiconductor layers, and dielectrics and describe challenges for advancing the scale up and circuit integration of printed metal oxide transistors.

## 2. Fundamentals – Ink Design, Printing, and Film Conversion

### *2.1 Ink design for printed metal oxides*

Sol-gel metal oxide inks for printed transistors are typically formulated by dissolving metal salt precursors (metal nitrates, chlorides, acetates, etc.) in an organic solvent or water.

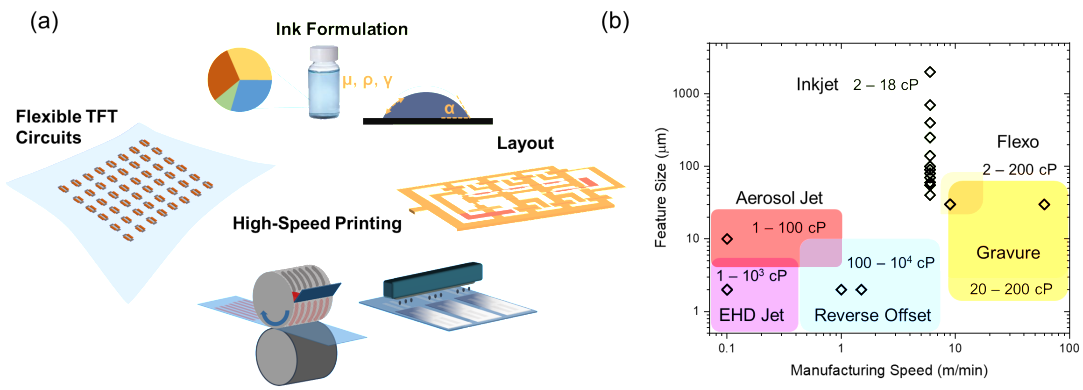


Figure 1: (a) Scheme depicting development of ink formulation, circuit layout, and high-speed printing methods including gravure and inkjet for fabrication of flexible thin film metal oxide transistor circuits. (b) Map summarizing printed feature size, manufacturing speed, and viscosity range for literature demonstrations of printed metal oxides formed by different printing methods. Colored regions denote the typical range of resolution and speed. Symbols denote the specific size and speed demonstrated experimentally in printed metal oxides to date. *Speed of inkjet printing extrapolated based on the assumption of industrial-scale multinozzle jetting.

The metal salts dissociate in solution, resulting in a coordination complex forming between the metal cation and solvent molecules. For example, when using $H_2O$ as the solvent, metal ions such as In can be fully solvated with water molecules as the nitrate anions are displaced[10]. The full dissociation of the nitrate anion has been cited as one possible explanation for its superior conversion to metal oxides[10]. We note that the sol-gel method offers a simple but essential advantage, namely, the ability to freely adjust film stoichiometry by tuning precursor concentration, for example a 7-1-2 $InGaZnO_x$ formulation or a 9-1 $In_2O_3$:Sn[11]. Additives to the ink are also used as fuel to enhance combustion reactions[12] (e.g. urea, acetylacetone, etc.) or provide additional oxidative power (e.g. $HClO_4$)[13] for completing sol-gel conversion at lower temperatures.

The solvent system and concentration modulate the fluid mechanics of sol-gel metal oxide inks, determining their suitability for high-volume printing technologies such as inkjet and gravure. Figure 1b illustrates a summary of several leading methods for printing metal oxide thin films, providing a comparison of the suitable viscosity range, patterning resolution, and speed demonstrated in literature (See Figure S1 and Table S1 for an annotated list of these parameters). Inkjet is an ideal digital manufacturing method for patterning low mass-loading, inviscid sol-gel inks (< 20 cP) where as roller-based methods such as gravure, flexography, and reverse offset excel in printing fine features at high speeds using more viscous inks ( 20 – 200 cP). The open symbols mark the patterning performance demonstrated in literature specifically for printed metal oxides while the shaded regions indicate the broader range over which each

technique is capable based on printing physics studies performed with other inks (polymers, nanoparticles, etc.). This comparison emphasizes the need for continued development of these roller-based methods that can exceed the throughput of nozzle-based methods (e.g. electrohydrodynamic jet and aerosol jet) by several orders of magnitude.

Recent advances in high-resolution inkjet printing of metal oxides have shown that stable jetting demands a balance of viscosity and surface tension that can be expressed in terms of the Weber number ( ! " $= \frac{\$\%^{\&'}}{(}$) and the Capillary number ( ) * $= \frac{+\%}{(}$) with droplet velocity (,), viscosity (-), density (1), droplet size (2) and surface tension (3). High speed and large droplets lead to inertial effects during jetting, causing formation of satellite droplets landing outside the intended feature. Figure 2a shows an example of the jettable window of two high performance sol-gel inks, as well as the jetting waveform and stroboscopic images of the droplets after firing. We note that most inkjet inks have a viscosity of 2 cP - 15 cP, but that inks

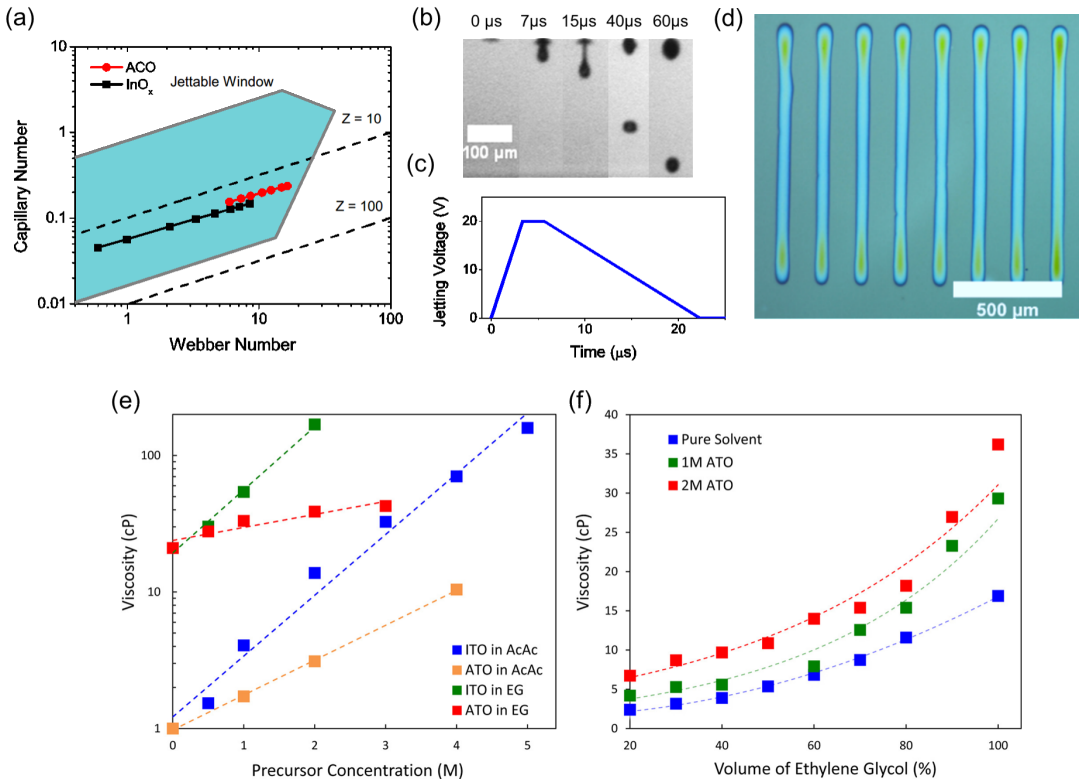


Figure 2: (a) Aluminum-doped CdO (ACO) inks plotted on a Capillary (*Ca*) number vs. Weber (*We*) number diagram with empirically determined jettable window shaded in grey and Z numbers 10 and 100 indicated by dashed lines. b) Stroboscopic snapshots of ACO droplets jetted from the piezoelectric print head by the corresponding jetting waveform. c) Inkjet nozzle voltage waveform for jetting aqueous inks with a common drop on demand inkjet printer (DMP 2831). d) Array of inkjet-printed conductive lines. Parts a-d are reproduced from Ref. 19. (e) Viscosity of sol-gel inks measured with rotary viscometer at a shear rate of 15 $s^{-1}$ for ITO ($SnCl_2$, $In(NO_3)_3$) and ATO ($SbCl_3$, $SnCl_2$) dissolved in acetylacetone (AcAc) or ethylene glycol (EG). (f) Viscosity vs. solvent composition for ethanol/ethylene glycol mixed ATO inks. Parts e,f are reproduced from Ref. 16.

on the margins of this range can still be jetted by adjusting the droplet dimensions, firing waveform, and surface tension. For a detailed phenomenological study of this behavior, we refer the reader to Derby, et al. [14]. As shown in other recent works developing inkjettable metal oxide inks, the control of the jetting voltage provides a second knob for tuning the droplet sizes and velocities for achieving stable jetting[15].

Viscosity and surface tension of metal oxide inks can be designed based on the concentration of solutes of sol-gel precursors[16] as well as the ratio of solvents. For example, viscosity of a simple metal nitrate solution in an organic solvent (e.g. acetylacetone) can be varied from 1 - 150 cP through high-concentration (5M) loading of $In(NO_3)_3$[16], (Figure 2e). Similarly, the viscosity of $Al(NO_3)_3$ in 2-methoxyethanol (2ME) can be adjusted from 2cP to 78 cP by via tuning concentration from 0 to 1.6 M[17]. This tuning provides a broad range for methods from gravure to flexography[17,18] as well as inkjet[19,20]. Solvent composition provides additional control over viscosity and surface tension. Figure 2f illustrates how viscosity of an ethanol and ethylene glycol (EG) ink can be tuned based on the percentage of higher viscosity EG, providing suitable rheology for printing high-resolution conducting oxide electrodes[16].

Ink spreading and formation of printed patterns also depend on the ink interaction with the substrate, specifically the difference between perfectly smooth substrates and those substrates that exhibit contact line pinning for a given ink. Sol-gel inks printed on extremely smooth substrates (e.g. $SiO_2$) have a problematic tendency towards, “inwards sliding of the three phase contact line," resulting in the shrinking and distortion of a printed pattern[21]. This phenomenon can be controlled by increasing viscosity with polymer additives[21], by inducing contact angle hysteresis to pin the contact line[22] or through printed hydrophobic banks that confine ink spreading[23]. The strategy of surface energy patterning has been used to form highly uniform electrodes for TFT arrays, but requires the tradeoff of several less scalable process steps including spin coating, plasma treatments, and high temperature anneals[23].

Recent progress in printed metal oxides has also targeted ink design for addressing the coffee ring artifact, a thick deposit at the edge of printed lines and films formed while the center remains much thinner. Figure 3a,b depict surface profiles of printed metal oxide droplets exhibiting the coffee ring effect. The coffee ring is particularly important for controlling the thickness of these printed layers such as gate insulators, for which thin regions present defects at which dielectric breakdown and leakage can occur. The roughness of the coffee-ring deposits themselves are also problematic, causing issues for the continuity of subsequent layers—an important issue for thin film transistors consisting of four consecutive printed layers (Figure 3c). In some recent cases, however, the non-uniformity of the coffee ring effect has been utilized

for patterning high performance TFTs that utilize the thicker edge regions effectively as extensions of the source drain electrodes[24].

Coffee rings form due to accelerated evaporation rate at the edge of a printed feature, inducing outward convective flows that deposit solute and result in rim deposits. Recent literature has provided several effective strategies for mitigating the coffee-ring effect, for example, by adjusting the substrate surface energy and increasing contact angle hysteresis[25], modulating the drying rate with substrate temperature control[26], and increasing the ink viscosity to slow convective flows[16]. The first and second strategies have been widely applied to sol-gel inks[22], but the increasing viscosity can be challenging for printing ultrathin films with lower mass-loading. Higher boiling point solvents can be used, but these also require higher temperature annealing to decompose[16,21]. It is worth noting that metal oxide inks based on organic solvents can exacerbate the coffee-ring effect due to an increase in the surface tension as a function of increasing concentration. The positive surface tension gradient from the inner to outer edge where the concentration is higher accelerates coffee ring formation. There is, though, the possibility to invert this effect with aqueous inks, which naturally form dome-shaped profiles due to their negative surface tension gradient with concentration[19].

One additional challenge for printing channels and dielectrics is achieving ultrathin films (< 20 nm) necessary for high gate capacitance and electrostatic control of conductive channels such as $InO_x$ and $InZnO_x$. This is essential for producing TFTs with low operating voltages[17,20,27] and for leveraging the faster conversion of ultrathin films[28]. Ultrathin films of oxides can be achieved with low concentration inks by methods such as inkjet[19,29], flexography[18,30,31], and gravure[31,32]. Scaling droplet size using smaller inkjet nozzles provides an approach to retain the benefits of viscous inks for uniform pattern formation while keeping film thickness low[20]. Finally, we highlight two considerations for high-speed printing,

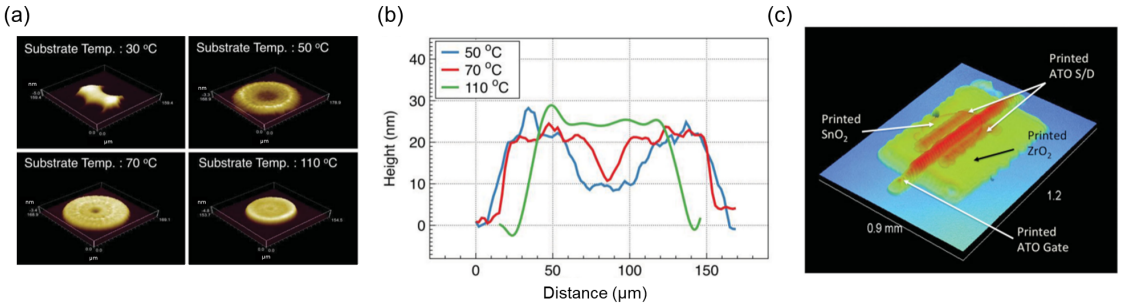


Figure 3: (a) Inkjet-printed droplet morphologies for sol-gel metal oxide inks exhibiting dewetting, coffee ring formation, and uniform films at various substrate temperatures (30 ˚C – 110 ˚C). (b) Line profiles showing thicker edge deposits from coffee-ring effect at low substrate temperatures. 3D surface profile measured by optical profilometry for a fully inkjet-printed oxide transistor based on sol-gel metal oxide inks. This figure is reproduced from Ref. 22.

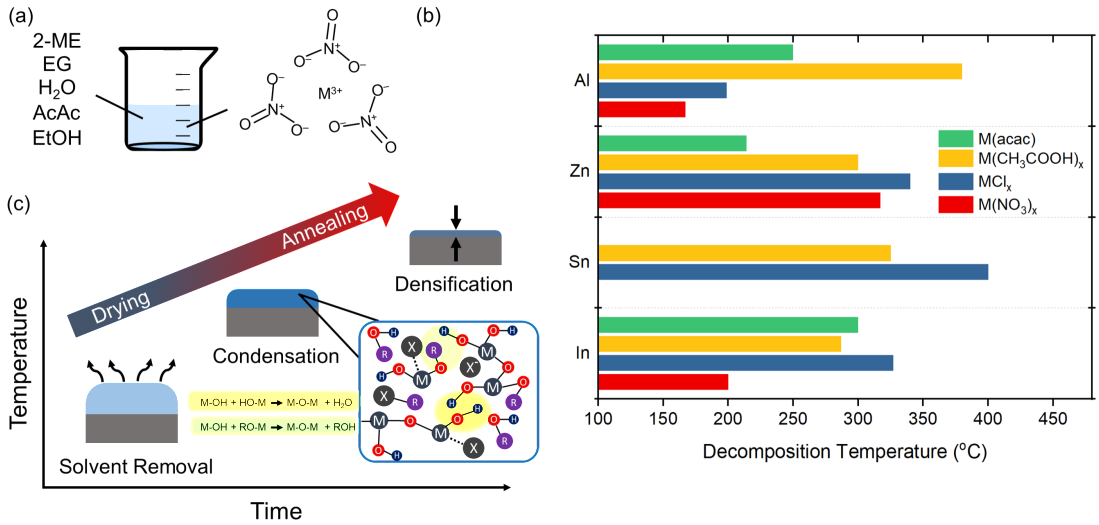


Figure 4: (a) Scheme for formulation of printed metal oxide sol-gel inks based on solvents (left) mixed with metal salt precursors (right). (b) Metal salt decomposition temperatures by precursor type. (c) Sol-gel formation process involving drying, condensation, and densification of the solid metal oxide thin film. Part c is reproduced from Ref. 39.

specifically high frequency and multinozzle jetting[20], which are attractive approaches to mitigate coffee-ring and other artifacts occuring in laboratory scale single nozzle printing. Ink design for roll-based printing with flexography and gravure generally require higher viscosity inks in the range of 20 – 200 cP for patterning fine features[33]. These higher viscosity inks are also effective for mitigating the coffee-ring effect by slowing convective flows from the edge to center of printed features.

### *2.2 High-Resolution Printed Oxide Transistors*

The printing resolution for patterning metal oxide transistors is also essential for determining whether down scaling of the channel length and upscaling of operating frequency to the MHz-range[34] or even GHz-range are achievable. Device as well as circuit-level performance are a strong function of material properties such as electronic mobility but also depend critically on geometric device parameters such as the channel length and parasitic capacitances, which can be minimized through single-micron-scale, high-resolution printing[34]. Short channel metal oxide transistors have been printed via inkjet by using means such as surface energy patterning to pattern finer features than otherwise possible based on the droplet size[35,36]. Methods such as flexography have also been utilized more recently for short channel device fabrication by roller-based methods for making 10 μm-scale channel length $In_2O_3$ transistors, albeit also using an indirect subtractive method of resist patterning by reverse offset[37]. Fully additive patterning of high performance metal oxide materials remains a challenge that offers a high potential payoff in terms of DC and AC device performance, but

will require further development of inks and processing by high-resolution printing methods such as gravure printing that can approach single micron linewidths[34].

### *2.3 Chemical Conversion, Annealing, and Crystallization of Printed Metal Oxides*

Figure 4a summarizes a typical composition of sol-gel precursor inks consisting of a solvent, often a glycol ether such as 2-methoxyethanol or ethylene glycol. This solvent is mixed with the precursor salt, for example, a metal nitrate ($M^{x+}(NO_3)_x$), chloride ($M^{x+}(Cl)_x$), acetate ($M^{x+}(C_2H_3O_2)_x$), or acetylacetonate ($M^{x+}(C_5H_7O_2)_x$), as shown in Figure 4b, which plots the decomposition temperatures for precursors used for common metal oxides such as $Al_2O_3$, ZnO, $SnO_2$, and $In_2O_3$. Metal nitrates offer substantially lower decomposition temperatures than other metal salts (Figure 4b), providing an efficient synthetic pathway to a range of dense metal oxide films, as detailed in a recent review by Cochran, et al. [38]. Metal nitrates also have the advantage of serving as an 'oxidizer' in combustion processing of sol-gels[12].

Printed sol-gel films require energy to drive conversion into the solid state oxide. The solvent and solute both determine the thermal budget for this transition. The chemical conversion of metal oxides includes elimination and condensation reactions, as highlighted in Figure 4c, that convert the liquid film to a solid state oxide dominated by metal-oxygen-metal (M-O-M) bonding[39]. The condensation reactions form the M-O-M network by eliminating hydroxides and expelling $H_2O$ vapor. Elimination reactions produce a similar effect, densifying the M-O-M network while volatilizing precursor anions (acetates, etc.) or strongly coordinated solvent molecules such as glycol ethers. These condensation and elimination reactions can be driven to completion thermally or by photonic energy from ultraviolet (UV) photons[40].

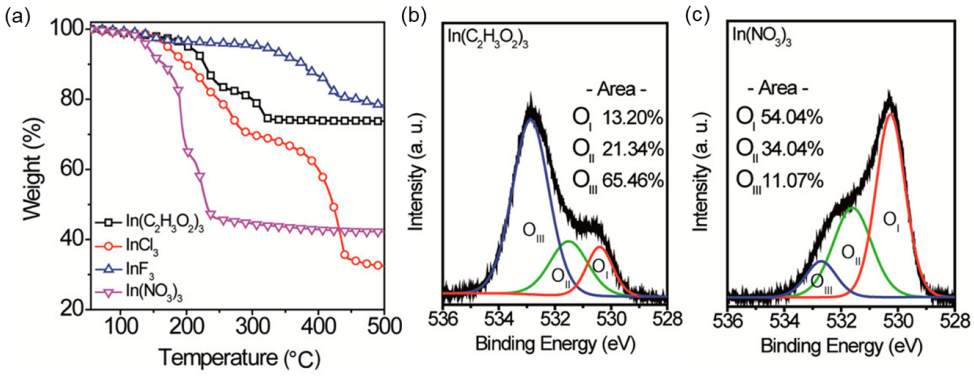


Figure 5: (a) Thermal gravimetry illustrating decomposition of sol-gel precursors to $In_2O_3$ including indium acetate (black), indium chloride (red), indium nitrate (purple), and indium fluoride (blue). XPS O1s spectrum for indium acetate (b) and indium nitrate (c) showing M-OH dominated bonding ($O_{11}$, $O_{111}$) vs. stoichiometric M-O bonding ($O_1$) , respectively. This figure is reproduced from Ref. 10.

The impact of incomplete sol-gel conversion can be observed through methods such as thermal gravimetry (TGA) and x-ray photoelectron spectroscopy (XPS) analysis of solution processed $In_2O_3$ shown above in Figure 5[10]. TGA clearly shows the favorable mass-loss profile of nitrate precursors occurring below 250 ˚C, while chlorides and acetates, for example, require higher temperatures (300-400 ˚C). XPS as well as Raman spectroscopy shows the identity of the chemical residues (N, C, Cl, etc.) as well as M-OH species that can remain trapped in sol-gel films, shown in the O1s peaks in Figure 5b,c. M-OH species are a natural consequence of sol-gel processing if the condensation reaction does not proceed to completion. The higher binding energy peaks (blue) show the substantial chemical difference between a film formed from nitrate and acetate precursors. OH content in the film is essential because Hydrogen in multiple potential defect species ($H_i$ or $H_o$) has been observed to be electronically important in oxides such as InZnO. For example, Socratous, et al. proposed that shallow dopant states induced by these H-species could serve an important role in oxide semiconductors of filling acceptor states near the CBM[41]. XPS characterization of alloyed semiconductors such as IGZO and dielectric materials such as $AlO_x$ shows similar behavior, with low-temperature processed sol-gel films' O1s peaks dominated by M-OH bonding while films annealing with advanced methods such as deep-UV-annealing and microwave annealing being dominated by M-O peaks[42].

Rapid deposition by printing necessitates consideration of the processes of drying and annealing required to form functional metal oxides. This is essential for integration of high-speed processing and use of roll-to-roll (R2R). In the majority of sol-gel metal oxide publications, rapid printing processes have been followed by long one hr anneals to densify the film and eliminate precursor residues that detract from electronic performance. A recent study by Marks, et al. addressed the question of how fast sol-gel metal oxides could be converted, considering the need to dry and then anneal by combustion processing[28]. This study determined that the time scales for film drying alone are approximately 60 s while the time for condensation reactions for densification was 10-100 s for ultrathin (< 3 nm) films and substantially longer for films 5-20 nm thick.

Methods to photochemically accelerate sol-gel conversion include photonic methods such as intense pulsed white light (IPL), deep-UV (DUV) annealing, and laser spike annealing. These techniques have shown the potential to dramatically enhance performance of low-temperature processed oxides[43]. These methods leverage UV for decomposing precursors as well as broadband illumination delivered as rapid pulses heating the substrate surface. The combination of heating with UV has been proven particularly effective at 150 – 200 ˚C.

Leppäniemi et al. showed via x-ray reflectivity measurements (XRR) that UV annealing contributes to forming substantially denser $In_2O_3$ films with higher mobility at these temperatures[29]. Intense pulsed white light has also been shown to effectively convert films of IGZO sol-gels by T.H. Yoo, et al. in 2014[44]. The intense pulsed light method provides opportunities for self-aligned patterning through selective curing of films on opaque electrodes. This method has recently been applied by Daunis, et al. for fabricating high quality $ZrO_x$ dielectrics on plastic substrates[45] and by Regoutz et al. for fabricating $In_2O_3$ films on plastic at low temperatures[46]. Although it requires rastering, laser spike annealing has been demonstrated using a near infrared laser ($\lambda \sim 1064$ nm) to drive conversion of printed IGZO at low temperatures[47]. Similarly, excimer laser annealing has improved performance of $AlO_x$ sol-gel dielectrics by inducing a lower temperature (150 ˚C), faster combustion reaction[48] without causing crystallization that might otherwise increase leakage current. Collectively, these state-of-the-art photonic annealing methods provide a path towards rapid processing of oxides at plastic-compatible temperatures, a key challenge in this field.

The crystallinity of printed oxides is an essential consideration for determining their performance as semiconductors and as gate dielectrics. In the case of $In_2O_3$, for example, polycrystalline films deposited by sputtering and atomic layer deposition can exhibit ultrahigh mobility above 100 $cm^2/Vs$[49,50]. Thermally-induced crystallization of vacuum deposited films ($In_2O_3$, ITO, $InGaO_x$) occurs readily upon annealing at 150 – 200 ˚C[51], resulting in a 300 – 20 400 % increases in mobility beyond that of amorphous films. Printed sol-gels of semiconducting

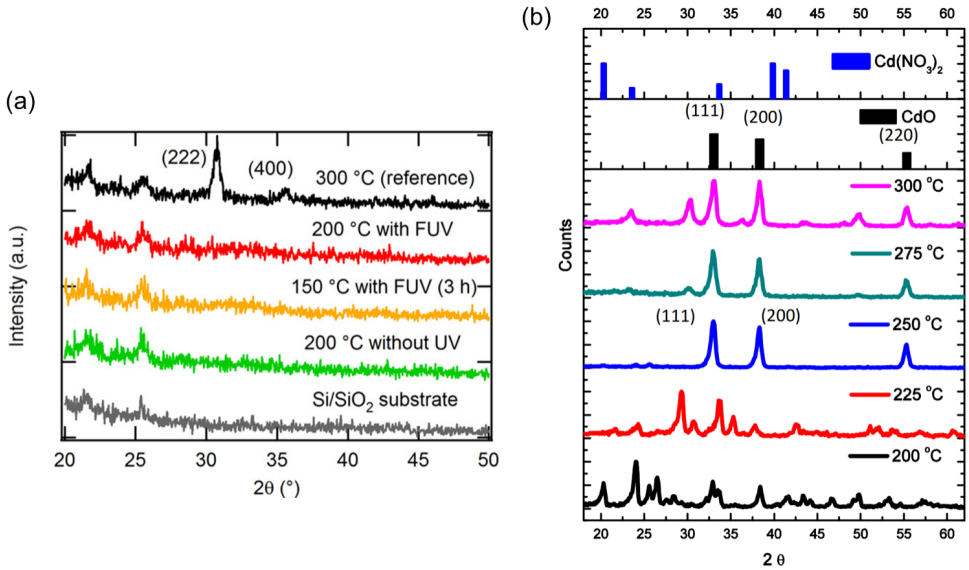


Figure 6: (a) X-ray diffraction (XRD) spectrum of inkjet-printed $In_2O_3$ formed from organic solvent inks (a). XRD spectra of CdO films formed from aqueous inks (b). Part a is reproduced from Ref. 29. Part b is reproduced from Ref. 19.

oxides can also be crystallized in this temperature range. $In_2O_3$ has also been observed to crystallize into the cubic phase at temperatures as low as 200 ˚C[52]. Interestingly, dilute inks resulting in ultrathin films of $In_2O_3$ (2-5 nm) tend to slightly suppress crystallization of $In_2O_3$ until higher temperatures[53]. Solution-processed ZnO based on aqueous inks has been observed to crystallize at temperatures around 180 ˚C[54] while solution-processed $SnO_2$ can be crystallized at approximately 200 ˚C using NaOH surface treatments[55].

Ink design can suppress or enhance crystallization of printed oxide films. The inclusion of additives with higher boiling point designed to stabilize the ink, such as ethylene glycol (EG) can have the effect of suppressing crystallization until 300 ˚C[29], (Figure 6a). Without the influence of organic solvents, we find in our study of carbon-free aqueous inks that crystallization occurs near 225 ˚C following the decomposition of metal nitrates[19] and the conversion hydroxide to the oxide phase. Figure 6b illustrates the sol-gel crystallization into cubic CdO. Although Cd-based TCOs present risks due to their high toxicity and potential for adverse environmental effects[56], these results demonstrate a more general principle regarding the advantage of carbon-free sol-gel ink formulations. Low temperature conversion of aqueous inks was similarly demonstrated by Myers, et al., to enhance the low temperature processing of ZnO channels[57]. Also of note for printing flexible electrodes is that heavy doping, for example, with 8 at. % of Al can amorphize ternary oxides such as ACO[19]. Low-temperature processing methods for dielectrics, however, have focused on maintaining the amorphous phase rather than inducing crystallization. For example, studies of $AlO_x$ have shown that it is possible to achieve the target film composition (M-O vs M-OH bonding) without causing crystallization[42].

## 3. Device Integration and Electronic Transport

### *3.1. Electronic Transport in Printed Metal Oxide Semiconductors*

Printed metal oxide transistors have been demonstrated with channels comprised of various n-type semiconductors including $In_2O_3$, $SnO_2$, $Ga_2O_3$, and ZnO, as well as alloys of these constituent oxides. The binary oxides such as $In_2O_3$ are generally highly conductive, requiring precise thickness control to achieve transistors with a combination of high $I_{on}$ / $I_{off}$, steep turn on, and high mobility. In fact, most recent high-performance printed $In_2O_3$ and $InZnO_x$ TFTs have optimal channel thickness of 8 – 15 nm[19,20,29–31,52]. Similarly, high-mobility printed $SnO_2$ TFTs have ultrathin channels around 10 nm thick[22,58,59]. Outside of this range, ultrathin channels below 5 nm exhibit lower mobility while thicker channels (> 25 nm) have worse off-state performance[58].

Multinary semiconducting oxides such as $InGaZnO_x$ (IGZO) offer the advantages of enhancement mode operation and the ability to achieve smooth films in the amorphous phase[60],

reducing interface roughness. A unique feature of printed IGZO channel materials is their ability to achieve high mobility (e.g. 5 $cm^2/Vs$) while suppressing oxygen vacancies, leading to turn-on near 0 V[61]. These characteristics have been associated with tighter distributions of characteristics such as the mobility and the threshold voltage in printed IGZO TFTs[21]. Printed IGZO channels achieve optimal performance for thicker films in the range of 20 – 60 nm[62], although there is one report of ultrathin printed IGZO channels less than 10 nm thick[63]. Quaternary semiconducting oxides such as $InZnSnO_x$ (IZTO) based on Sn rather than Ga can offer similar benefits of the amorphous phase, but generally yield more conductive channels with higher mobility than IGZO[64]. The additional doping of Ga into these mixtures can improve stability while maintaining high electron mobility[65]. Finally, it is also possible to print indium-free formulations for channels based on semiconductors such as $ZnSnO_x$ (ZTO) that exhibit high performance but rely only on lower cost precursor materials with higher earth abundance[66].

Recent theoretical work has provided a basis for modelling transport in solution-processed oxide semiconductors. For example, Wang, et al. have modeled the effects of trapped carrier scattering[67] and interface roughness[68] on the mobility of solution processed metal oxides such as $ZnSnO_x$ (ZTO), showing that even a 1 nm RMS roughness limits the band mobility. Interestingly, they show a connection with the dielectric material selection, finding that high-k dielectrics provide a reduction in interface roughness scattering due to the lower interfacial electric field[68]. We highlight that this factor could be of importance for printed oxide TFTs that naturally present rougher interfaces than vacuum deposited films. Another specific result of their recent modeling[67,67] has been to show the dependence of metal oxide TFT mobility on the sheet carrier density – specifically the beneficial role of electrostatic screening of trapped carrier scattering. These augmented models for transport in disordered metal oxide semiconductors provide a basis for designing improved metal oxide TFTs.

Bias-stress stability, which quantifies the shift in the threshold voltage with the application of constant gate bias ($V_{gs}$), remains a substantial challenge for circuit applications of printed metal oxide transistors. Several recent works have reported bias-stress statistics for printed metal oxide transistors that fall in the range of a $\Delta V_{th}$ of approximately 10 % of the stress voltage[20,23,69], a value 10X greater than those observed for state of the art IGZO channels passivated by vacuum-deposited $SiO_2$ layers[70]. Previous works utilizing printed high-k dielectrics such as $Al_2O_3$ with printed oxide semiconductors have also generally reported the degradation in subthreshold slope with additional positive (PBS) or negative (NBS) bias stress[17,20], consistent with electron trapping at the channel dielectric interface. Passivation of the back channel interface of $SnO_2$ TFTs with $Y_2O_3$ has recently been shown to mitigate bias-

stress effects by controlling the oxygen vacancy concentration at the back channel surface[71]. Similar approaches can likely be applied to improve the operational stability of printed metal oxides as printing processes are extended to these inorganic passivation layers that can effectively block gas diffusion.

Unpassivated back channels of metal oxide TFTs exhibit greater variability in their threshold voltages, larger hysteresis and poor bias-stress stability associated with traps from adsorbed $H_2O$ at this interface[72]. Passivation layers applied to the back channel, for example, printed low-temperature UV-curable organosilicates, can reduce hysteresis and improve bias-stress of printed $In_2O_3$ transistors[73]. Among other options, poly (methylmethacrylate) (PMMA) has also been demonstrated to form a stable interface for effectively passivating the back-channel of metal oxides such as IZO[74] and $In_2O_3$[20].

### *3.2 Heterojunction Metal Oxide Channel Architectures*

Recent work in solution-processed metal oxide transistors has shown a substantial performance boost from integrating multilayer heterojunction channel architectures. These works suggest the important role of the heterointerface for producing devices that can improve both the on-state and off-state performance while enhancing bias-stress stability by passivating back-channel interface. Heterojunctions based on ultrathin semiconducting oxide layers (3-7 nm) have become a leading method for achieving higher performance at plastic-compatible temperatures below 200 ˚C, leading to demonstrations of high mobility (30 $cm^2/Vs$) using multilayers consisting of multiple wide bandgap oxides such as $In_2O_3$, $Ga_2O_3$, and ZnO[75]. A few recent works have translated these heterojunction multilayer channel designs into printed device architectures. Liang, et al. in 2019 reported printed bilayer heterojunction channels based on an inkjet-printed stack of 10 nm of $In_2O_3$ / and 7 nm of IGZO, which showed the benefit of higher on-state performance ($\mu_{ave}$ ~ 14 $cm^2/Vs$) and improved subthreshold slope compared with channels based on pure $InO_x$ or pure IGZO[69]. The authors note how the heterostructure additionally provided the advantage of confining the subsequent IGZO ink via a contact-line pinning effect. S.H. Lee show similar results for inkjet-printed dual active layer TFTs with ZTO and $In_2O_3$ heterostructure channels, observing higher mobility, improved subthreshold slope for the dual layer oxide semiconductors[76]. Finally, a recent work by Shao, et al. showed inkjet-printed heterostructures consisting of highly conductive $In_2O_3$ coated with IGZO to form multilayer channels with high mobility ($\mu_{ave}$ ~ 17.7 $cm^2/Vs$), minimal hysteresis, and impressively low variance[77]. Additional device modeling should be applied to rationalize the design of optimal multilayer channels.

### *3.3 Printed Electrodes for Metal Oxide Transistors*

Recent work includes progress towards printing the source / drain and gate electrodes, essential to fabricating the entire device structure with scalable and low cost processes. There is a particular need to develop chemically stable printed electrodes for oxide transistors, since most prior literature has utilized vacuum-deposited metal electrodes patterned by photolithography. We also note the heightened need for deeper understanding of printable electrode formulations because the source and drain present the critical dimension of printed transistor, defining the channel length as well as the parasitic gate overlap capacitance[34]. Transparent electrodes additionally match the transparency of metal oxide channels and dielectrics, while vacuum-evaporated metals nullify those benefits.

There is a continued need for chemically resilient conductors that can serve as source / drains as well as gate electrodes. Metal nanoparticle based inks that have been utilized in organic transistors are typically composed of Ag and have high conductivity, but generally demonstrate poor stability interfaces with metal oxide semiconductors[78]. There is at least one notable exception reporting low contact resistance to $In_2O_3$ achieved using a PEI polymer doped interfacial $In_2O_3$ layer to a printed Ag NP[79]. Carbon nanomaterial based conductors provide a promising alternative. Secor, et al. demonstrated in 2016 that inkjet-printed graphene inks can serve as a chemically stable alternative to metal and transparent conductive oxide (TCO) inks, offering long-term stability and the potential to achieve low-resistance interfaces when embedded between multiple printed IGZO layers[78].

Sol-gel TCO inks based on materials such as indium tin oxide (ITO) are a natural choice for printed electrodes given their chemical similarity to the inks formulated for semiconducting channel layers. However, initial demonstrations of inkjet-printed sol-gel electrodes based on materials such as IZO required high temperature annealing up to 500 – 600 ˚C and offered only 100 kΩ - 1 MΩ sheet resistance[80], insufficient for high performance TFTs with on-state channel resistance in the 1-10 kΩ range. More recently, Y. Li, et al. have shown ITO sol-gel formulations based $In(NO3)_3$ that provided high enough conductivity for integration of fully printed oxide TFTs, suitable for high-mobility (3-5 $cm^2/Vs$) TFTs when using anneals at 350 ˚C. Similarly, our previous work by J. Jang, showed that an Sb-doped $SnO_x$ sol-gel (ATO) provided high stability and conductivity for full printed oxide TFTs with mobility up to 11 $cm^2/Vs$, although requiring anneals at 400 – 500 ˚C[22]. These works demonstrate how the sol-gel TCO electrodes can effectively limit the scaling down of the thermal budget of printed metal oxide transistors.

We recently demonstrated a strategy for reducing process temperatures by utilizing aqueous inks for printed oxide transistors[19] (Figure 7a,b). Our formulation used nitrate

precursors to print aluminum-doped CdO electrodes (ACO) with high conductivity at low processing temperatures (200 – 250 ˚C) compatible with polymer substrates (Figure 7c). These printed electrodes yielded low contact resistance to aqueous printed $InO_x$, leading to high-mobility TFTs (up to 19 $cm^2/Vs$) with minimal hysteresis and steep turn on (Figure 7d). Aqueous inks boost the conductivity compared with organic solvent inks, lowering the thermal processing limit for printed source / drain electrodes. Although additive printing processes result in high material utilization and a reduction in heavy metal-contaminated waste streams otherwise caused by subtractive etching, there remains a need to develop safe and low-cost alternatives for low-temperature printed TCOs that are also compatible with high quality dielectrics processed at low temperatures via aqueous inks ($AlO_x$) based on metal nitrates[81]. Particle free, sol-gel solutions offer one approach to limit the health risks of aerosolized nanoscale powders present during processing.

Given the dominance of indium-based semiconductors and electrodes in the printed metal oxide literature, we address the frequently cited limitation posed by the perceived scarcity of Indium. As a raw material input to printed and flexible electronics, the bulk price of indium ($200 / kg) is expected to be non-limiting for devices using ultrathin oxide semiconductor films that are < 20 nm thick and occupy a small fraction of the total area. For perspective, a large 1 x 1 m display with 10 nm $In_2O_3$ channels would require just 1 mg of indium (~ 0.01 USD) – global production of indium is approximately 1000 tons/year[9]. Silver, by comparison, is printed at micron-scale thicknesses and costs 3-4X as much as indium at time of publication, though its cost has not limited printed electronics broader commercial viability. If metals such as indium became limiting resources for technology such as displays, printed electronics would be well positioned relative to incumbent manufacturing technology because of its material high utilization rate compared with photolithography and subtractive etches. Based on these mitigating factors, we argue that indium's scarcity and cost may not necessitate indium-free semiconductors for printed TFTs.

### *3.4 Printed High-k Oxide Dielectrics*

A large majority of the printed metal oxide transistors reported to date has been using thermally grown $SiO_2$ dielectrics or, otherwise, spin coated metal oxides, but integration of printed metal oxides into large-area technologies necessitates development of appropriate printed dielectric technology. Most leading works in printed oxide TFTs have utilized inorganic high-k dielectrics such as $Al_2O_3$, $ZrO_x$, and $HfO_x$, etc, which offer high capacitance and high breakdown fields, often greater than 4 MV/cm. The high capacitance offered by high-k dielectrics has an important role, for example, in allowing effective gating of highly conductive channel materials

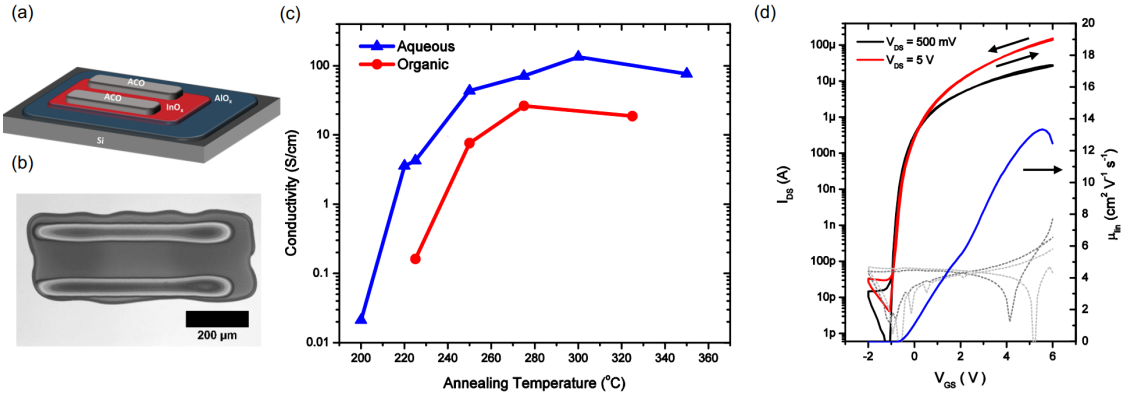


Figure 7: (a) Schematic of printed transistors with all aqueous inks forming semiconductor, electrodes, and dielectric layer. (b) Image of printed transistor with aqueous printed ACO source/drain eletrodes (c) Conductivity of inkjet-printed ACO electrodes with aqueous and organic (2-methoxyethanol as the solvent) precursor inks shown in blue and red, respectively. Reproduced from Ref. 19.

such as $SnO_x$[22] or ITO[82] and acting as a source of donor states for compensating bulk traps and improving electronic mobility in semiconductors such as ZnO[83].

Recent work has begun to incorporate these advantages of solution-processed high-k dielectrics with high speed printing processes for deeper device integration. UV-annealing has also become an essential tool for printing high quality high-k dielectrics at plastic-compatible temperatures. For example, in 2020, Carlos, et al. reported flexography-printed $AlO_x$ sol-gel dielectrics annealed at just 180 ˚C using DUV exposure (deuterium lamp) in a nitrogen glovebox, integrated into printed $In_2O_3$ TFTs with an operating voltage of just 2 V and a mobility of approximately 1 $cm^2/Vs$[17]. Similarly, we recently reported[20] printed $In_2O_3$ TFTs utilizing broadband UV exposure (high power metal halide lamp) to cure printed $AlO_x$ at 150 – 200 ˚C, with printed $In_2O_3$ semiconductors achieving linear field effect mobility of 12 ± 1.6 $cm^2/Vs$ and operation at 3 V, as shown in Figure 8. In our study as well as Carlos, et al.[17], UV exposure was found to improve dielectric breakdown, leakage, and dramatically reduce low-frequency dispersion in these printed high-k dielectrics, supporting the hypothesis that UV can aid low-temperature condensation and elimination reactions.

## 4. Persistent Challenges, Emerging Opportunities, and Applications

### *4.1 Printing Flexible Metal Oxide Transistors*

Progress towards low-temperature ink chemistries and annealing has allowed fabrication of printed devices on flexible substrates such as polyimide ($T_g$ ~ 300 ˚C). Initial demonstrations, for example, by J. Leppäniemi in 2015[30] of flexography-printed $In_2O_3$ semiconductors[17] have shown the potential for[84] high mobility (8 $cm^2/Vs$) and fabrication on polyimide (Figure 9a-e), but still required 300 ˚C annealing steps. Follow up work by Leppäniemi showed that far-UV annealing could also be used to lower the process temperature for printing TFTs on lower cost,

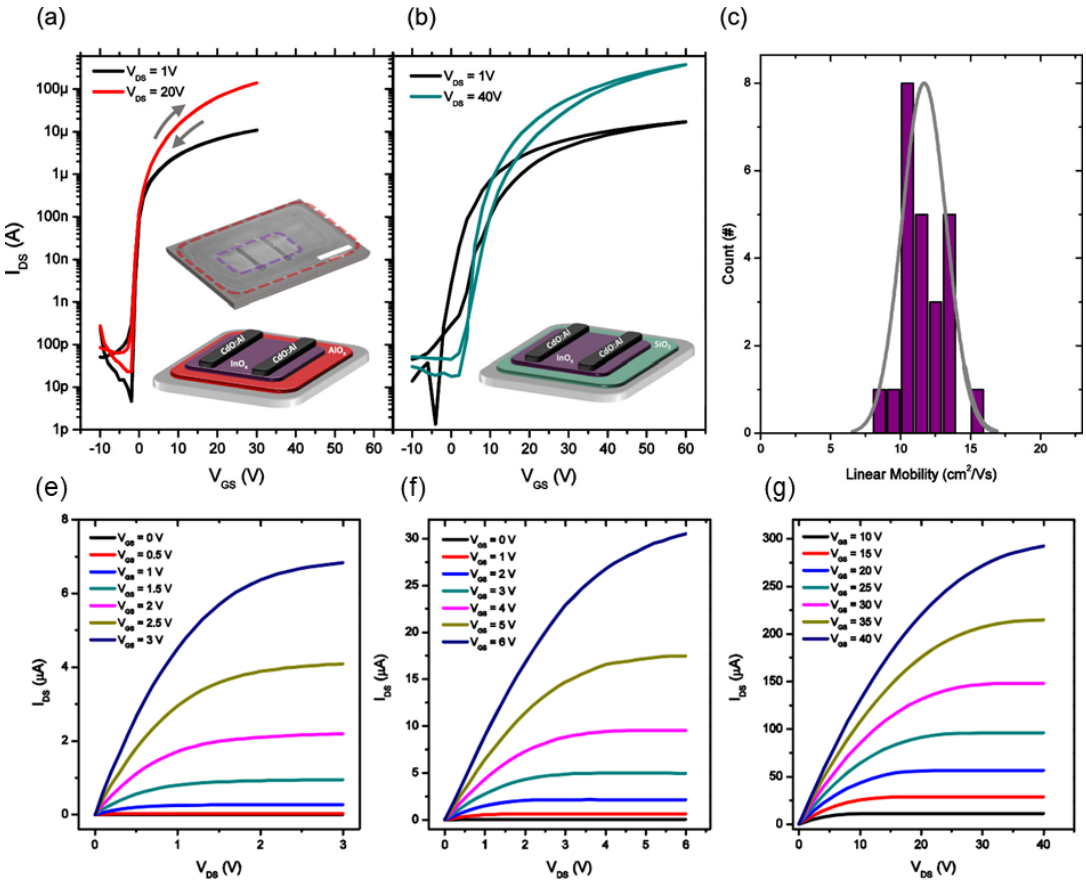


Figure 8: Transfer characteristics of $In_2O_3$ transistors with printed channels and printed electrodes with printed $Al_2O_3$ dielectrics (a) vs. thermally grown $SiO_2$ dielectric (b). (c) shows the linear mobility distributuion for devices with printed $Al_2O_3$ dielectrics. Output characteristics of printed $InO_x$ TFTs with $Al_2O_3$ dielectrics of $t_{ox}$ = 15 (e), 30 (f), and 200 nm (g). Reproduced from Ref. 20.

but thermally sensitive polyethylene naphthalate (PEN) at 160 ˚C[29], achieving a mobility of 4.3 $cm^2$/Vs. Finally, more recent work by Carlos, et al. showed $In_2O_3$ transistors printed on thin polyimide (38 μm) with printed dielectrics at 180 ˚C via UV-annealing can sustain cyclic bending at radii of 5 mm and below (Figure 9g), opening up flexible device applications[17]. However, despite this progress towards integration on plastic, there have been few works that print the full TFT stack, including electrodes. The first demonstration by Zeumault, et al. overcame this challenge by using F-doped $SnO_x$ electrodes for fully printed oxide TFTs on polyimide, eliminating evaporated electrodes[85]. A more recent demonstration by Singaraju, et al. achieved higher performance and lower voltages using an electrolyte gated $In_2O_3$ channel with graphene electrodes[84], (Figure 9h,i). The substantial performance gap remaining between rigid and flexible printed oxide transistors, however, highlights the remaining the need for further developing high conductivity printed electrodes and printed dielectric materials to improve printability of flexible devices.

Flexible metal oxide transistors are less strain tolerant than organic semiconductors, typically limited to approximately 1% bending strain before cracking and delamination occur. Printed oxides can, however, borrow from recent literature on spin coated metal oxides incorporating polymers to improve flexibility[86]. Wang, et al. recently demonstrated how 0.5 – 5 2% wt. of amino-polymers such as polyethyleneimine (PEI) can improve ductility of $In_2O_3$, enhancing its performance under bending strain. This approach could be promising given the tendency of polymer additives to improve the printability of sol-gel metal oxide inks and the uniformity of resulting films[87]. Another recent finding that could improve mechanical reliability of metal oxide TFTs is the discovery of the combination of ultrathin oxides in layered

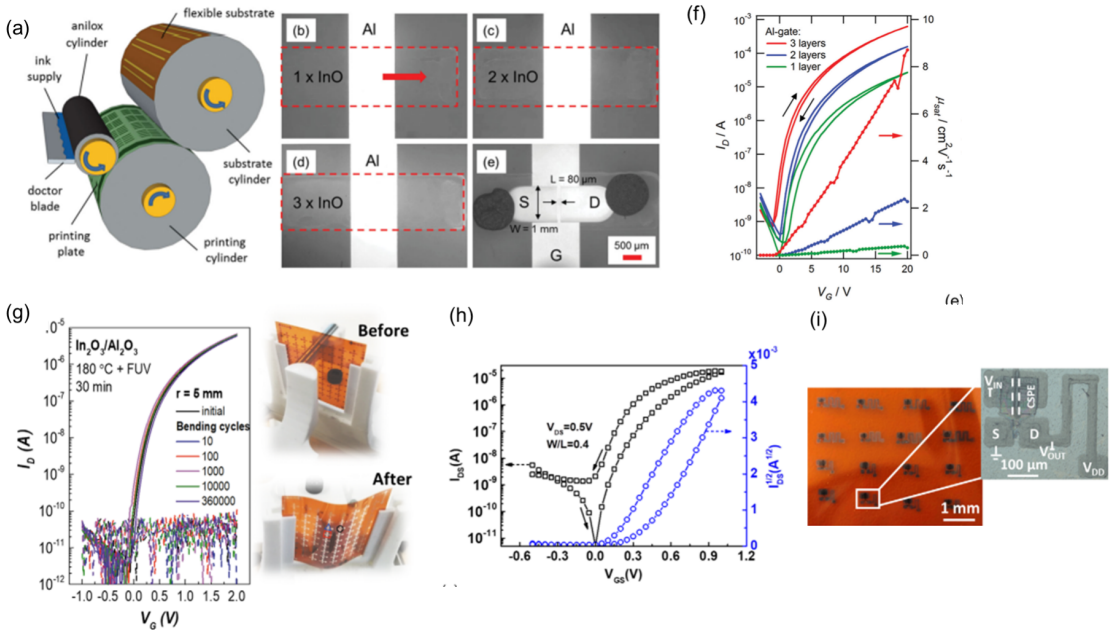


Figure 9: (a) Schematic depicting flexographic printing of indium nitrate sol-gels on polyimide flexible substrates to form multilayer $In_2O_3$ semiconductors (b-e) exhibiting transfer curves (f) with mobility up to 8 $cm^2/Vs$. Parts a-f reproduced from Ref. 30. (g) Transfer characteristics of printed $In_2O_3$ transistors on polyimide substrates processed at 180 ˚C using UV annealing. Part g is reproduced from Ref 15. (h,i) Low-voltage electrolyte gated $In_2O_3$ transistors printed on polyimide with printed electrodes comprised of graphene. Parts h,i reproduced from Ref. 79.

'superlattices' with self-assembled monolayers that reduce stress and improve performance under bending[88].

### *4.2 Liquid Metal Printing – A Rapid Approach to Fabricating 2D Metal Oxides*

The need for ultrathin films and low-temperature processing of flexible metal oxides motivates the consideration of a class of two-dimensional (2D) metal oxides that come from alternative synthesis methods that circumvent the limits of the sol-gel conversion process. 2D oxides fabricated from the spontaneously forming 1 - 3nm thick native surface oxides of low melting temperature metals[89] could offer a promising approach to improve material

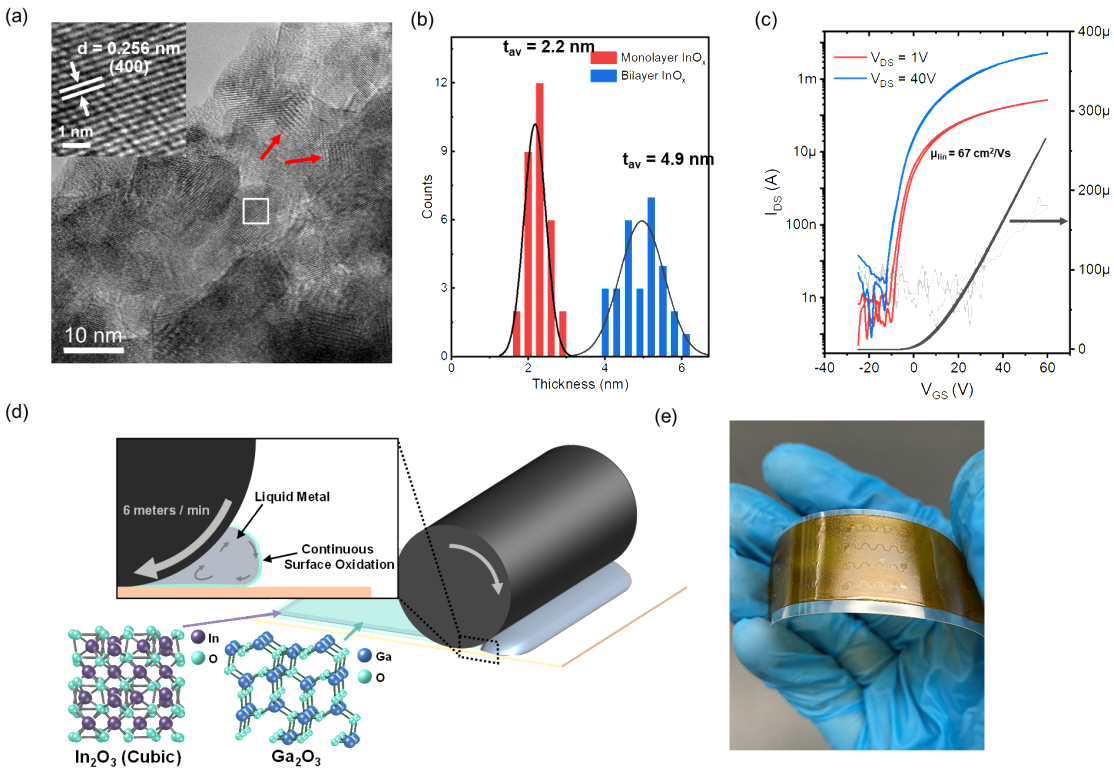


Figure 10: (a) Liquid metal printed 2D $In_2O_3$ crystalline morphologies observed by HRTEM, with red arrows highlighting overlapping crystallites displaying Moiré fringes. (b) Histogram of measured thicknesses for 2D $In_2O_3$ single layers (red) and double layers (blue). Single layer refers to a single surface oxide skin approximately twice the $In_2O_3$ unit cell size in thickness. (c) Transfer characteristic of champion 2D $In_2O_3$ transistor printed from liquid metals at 165 ˚C. (d) Roller-based continuous liquid metal printing (CLMP) for rapid deposition of superlattices of $In_2O_3$ and $Ga_2O_3$. (e) Transparent conducting 2D oxide superlattices printed on flexible polyimide. Parts a,b,c reproduced from Ref. 55. Parts d,e reproduced from Ref. 93.

performance while reducing processing time and temperatures used. Since 2017, this liquid metal printing process has been applied to synthesize a large variety of 2D oxides relevant to the fabrication of thin film transistors, including challenging materials such as p-type SnO[90]. The 2D surface oxides can be effectively transferred to a target substrate using van der Waals force to adhere large, $cm^2$ scale nanosheets only slightly thicker (~ 2X) than the unit cell size of $In_2O_3$. Liquid metal printed 2D ITO exhibits transmittance above 99% in the visible while providing $R_s$ ~ 1-5 kΩ/sqr and affording printability on flexible PEN substrates[91] at just 200 ˚C. Recently, this liquid metal approach has also been used to synthesize high-k $Sb_2O_3$ dielectrics with low leakage current density and extremely high capacitance[92]. This expanding material set and the inherently low process temperatures of liquid metal printing make it an attractive method for overcoming the fundamental limitations of printed metal oxide materials.

Our recent work in liquid metal printing of 2D oxides advances the droplet-wise process[91] towards a scalable approach for depositing large-area films, as illustrated in Figure

10. For example, polycrystalline $In_2O_3$ films can be spontaneously oxidized on molten In and transferred to a target substrate using a high speed roller-based form of van der Waals transfer[93]. The notable absence of precursor impurities (compared with sol-gel metal oxides) due to the *native* Cabrera-Mott oxidation process leads to the remarkable ability to use the ultrathin, functional 2 - 5 nm thick (Figure 10b) 2D oxide films as deposited, at which stage they are highly conductive as well as crystalline (Figure 10a) despite being processed in a total of less than 3 seconds. Figure 10 presents These films can be utilized for fabricating ultrahigh mobilty (67 $cm^2/Vs$) $In_2O_3$ transistors at temperatures < 165 ˚C with ideal transfer characteristics showing low hysteresis (Figure 10c)[53]. These 2D oxides can also be utilized for assembling heterostructures of multipler wide bandgap oxides ($In_2O_3$, $Ga_2O_3$, etc) for modulation doping to reach high conductivity films on polymer substrates including PEN and polyimide[93].

### *4.3 Principal Challenges – Uniformity and Complementary Channel Materials*

The device-to-device uniformity and the scaling of lateral dimensions (e.g. channel length) are essential for advancing the state of the art of printed metal oxide transistors. These are two of the most important barriers limiting performance of printed metal oxides relative to vacuum processed devices fabricated by methods such as sputtering. Threshold voltage variation is particularly important for allowing design of more complex circuits requiring matched device characteristics[94]. This issue motivates the selection of materials and processign methods that can reduce sensitivity to process variations and environmental effects that might enhance variability. It also motivates deeper study of the mechanisms behind spatial variation of printed devices, for example, effects related to the modulation of wetting and ink transfer.

Another challenge for circuit integration is the lack of high-mobility, hole-conducting metal oxides necessary for integrating complementary TFT circuits. Complementary logic circuits could offer higher integration density and lower quiescent power than can be achieved with unipolar TFT circuits[95], though we note that for certain analog applications such as physiological monitoring, unipolar IGZO devices offer competitive performance for low-noise amplification[96]. The synthesis of p-type oxides materials remain challenging but not impossible via solution-processing. Inkjet-printed $NiO_x$ TFTs have been achieved with mobility ~ 0.78 $cm^2/Vs$[97] using a nickel acetate sol-gel formulation, although this is among the few printed p-type oxide transistors which have been demonstrated. Printed p-type oxide TFTs based on nanoparticulate $Cu_2O$ inks have also been shown using electrolyte-gated architectures to integrate complementary circuits with n-type oxide TFTs[98]. Alternative synthesis by methods such as liquid metal printing can offer higher performance for fabricating phases such as SnO that are challenging to achieve by annealing traditional sol-gel metal oxides[90].

One recent trend in the display industry could offer a clue to solving the challenges of complementary printed metal oxide transistors. The demand for high-performance bipolar driving circuits in high resolution display backplanes has driven the development of hybrid processes utilizing both IGZO n-channel and p-type low-temperature polycrystalline silicon (LTPS) devices[99]. Along these same lines, we could imagine hybrid printed electronic circuits capitalizing on both high mobility n-type oxides and high mobility p-type organics. For example, high mobility small molecule p-type organic semiconductors can be used to form complementary logic circuits alongside $InO_x$/ZnO n-channels with balanced carrier mobility at the 10 $cm^2/Vs$ level[100]. There is the possibility to even consider combining p-type organics with n-type inorganic semiconductors within the same device architecture to design a single ambipolar transistor[101]. Low-temperature processing of metal oxides as well as the integration of polymeric additives in oxide films both promise to make these two material sets increasingly compatible.

## 5. Conclusions and Future Outlook

This paper provides a review of sol-gel ink chemistry, fluid mechanics of printed film formation, and strategies for designing the multiple material components of high-mobility metal oxide transistors. We have assessed recent advances in electrodes and dielectrics towards fully-printed architectures and discussed performance of flexible printed transistors. These results demonstrate how printing metal oxides requires a combination of advances in precursor formulation, thermal and photonic processing, and device engineering to obtain devices with ideal switching characteristics. Finally, we have highlighted pressing challenges facing the field, including device uniformity, mechanical flexibility, and low-temperature processing.

Looking forward, printed metal oxides can draw on progress in organic electronics, where researchers have pushed limits of printing speed and resolution to boost performance via micron-scale patterning with gravure and reverse offset. Indeed, these strategies for printing scaling channel lengths could help metal oxides reach their potential as a building block of high-frequency flexible circuits. Circuit implementations of printed metal oxides also dictate a renewed focus on operational stability, specifically the passivation of printed TFTs to mitigate bias-stress instabilities and strategies to reduce residual mechanical stresses. Development of low-temperature printed films by photonic annealing or liquid metal printing can improve flexibility and allow use of lower-cost polymer substrates beyond polyimide. Continued progress in these areas promises to enable emerging flexible electronics applications.

## Supplementary Material

Supplementary material is available including a full description of the literature reports summarized in Figure 1b.

## Conflict of Interest

The authors declare no conflict of interest.

## Data Availability Statement

Data sharing is not applicable to this article as no new data were created or analyzed in this study.


## Acknowledgements

This research was supported by the National Science Foundation Electronic and Photonic Materials program (Award #2202501).


## References


[1] J. Kwon, S. Baek, Y. Lee, S. Tokito, and S. Jung, Langmuir **37**, 10692 (2021).

[2] E. Pomerantseva, F. Bonaccorso, X. Feng, Y. Cui, and Y. Gogotsi, Science **366**, eaan8285 (2019).

[3] S. Yao, P. Swetha, and Y. Zhu, Adv. Healthc. Mater. **7**, 1700889 (2018).

[4] C. Zhao, Y. Zhou, S. Gu, S. Cao, J. Wang, M. Zhang, Y. Wu, and D. Kong, ACS Appl. Mater. Interfaces **12**, 47902 (2020).

[5] K.-J. Baeg, M. Caironi, and Y.-Y. Noh, Adv. Mater. **25**, 4210 (2013).

[6] K. Fukuda and T. Someya, Adv. Mater. **29**, 1602736 (2017).

[7] D. Ji, J. Jang, J.H. Park, D. Kim, Y.S. Rim, D.K. Hwang, and Y.-Y. Noh, J. Inf. Disp. **22**, 1 (2021).

[8] N. Münzenrieder, K. Ishida, T. Meister, G. Cantarella, L. Petti, C. Carta, F. Ellinger, and G. Tröster, IEEE Electron Device Lett. **39**, 1310 (2018).

[9] *Mineral Commodity Summaries 2022* (U.S. Geological Survey, Reston, VA, 2022), p. 202.

[10] Y.S. Rim, H. Chen, T.-B. Song, S.-H. Bae, and Y. Yang, Chem. Mater. **27**, 5808 (2015).

[11] Z. Chen, W. Li, R. Li, Y. Zhang, G. Xu, and H. Cheng, Langmuir **29**, 13836 (2013).

[12] M.-G. Kim, M.G. Kanatzidis, A. Facchetti, and T.J. Marks, Nat. Mater. **10**, 382 (2011).

[13] H. Chen, Y.S. Rim, C. Jiang, and Y. Yang, Chem. Mater. **27**, 4713 (2015).

[14] Y. Liu and B. Derby, Phys. Fluids **31**, 032004 (2019).

[15] S. Meyer, D.V. Pham, S. Merkulov, D. Weber, A. Merkulov, N. Benson, and R. Schmechel, ACS Appl. Mater. Interfaces **9**, 2625 (2017).

[16] W.J. Scheideler, J. Jang, M.A.U. Karim, R. Kitsomboonloha, A. Zeumault, and V. Subramanian, ACS Appl. Mater. Interfaces **7**, 12679 (2015).

[17] E. Carlos, J. Leppäniemi, A. Sneck, A. Alastalo, J. Deuermeier, R. Branquinho, R. Martins, and E. Fortunato, Adv. Electron. Mater. **6**, 1901071 (2020).

[18] J.E. Huddy, Y. Ye, and W.J. Scheideler, Adv. Mater. Technol. **7**, 2101282 (2022).

[19] W.J. Scheideler, R. Kumar, A.R. Zeumault, and V. Subramanian, Adv. Funct. Mater. **27**, 1606062 (2017).

[20] W.J. Scheideler, M.W. McPhail, R. Kumar, J. Smith, and V. Subramanian, ACS Appl. Mater. Interfaces **10**, 37277 (2018).

[21] S. Wu, Q. Zhang, Z. Chen, L. Mo, S. Shao, and Z. Cui, J. Mater. Chem. C **5**, 7495 (2017).

[22] J. Jang, H. Kang, H.C.N. Chakravarthula, and V. Subramanian, Adv. Electron. Mater. **1**, 1500086 (2015).
[23] Y. Li, L. Lan, S. Sun, Z. Lin, P. Gao, W. Song, E. Song, P. Zhang, and J. Peng, ACS Appl. Mater. Interfaces **9**, 8194 (2017).
[24] K. Liang, D. Li, H. Ren, M. Zhao, H. Wang, M. Ding, G. Xu, X. Zhao, S. Long, S. Zhu, P. Sheng, W. Li, X. Lin, and B. Zhu, Nano-Micro Lett. **13**, 164 (2021).
[25] Y.-F. Li, Y.-J. Sheng, and H.-K. Tsao, Langmuir **29**, 7802 (2013).
[26] D. Soltman and V. Subramanian, Langmuir **24**, 2224 (2008).
[27] L. Gillan, S. Li, J. Lahtinen, C.-H. Chang, A. Alastalo, and J. Leppäniemi, Adv. Mater. Interfaces **8**, 2100728 (2021).
[28] B. Wang, P. Guo, L. Zeng, X. Yu, A. Sil, W. Huang, M.J. Leonardi, X. Zhang, G. Wang, S. Lu, Z. Chen, M.J. Bedzyk, R.D. Schaller, T.J. Marks, and A. Facchetti, Proc. Natl. Acad. Sci. **116**, 9230 (2019).
[29] J. Leppäniemi, K. Eiroma, H. Majumdar, and A. Alastalo, ACS Appl. Mater. Interfaces **9**, 8774 (2017).
[30] J. Leppäniemi, O.-H. Huttunen, H. Majumdar, and A. Alastalo, Adv. Mater. **27**, 7168 (2015).
[31] D. Spiehl, M. Häming, H.M. Sauer, K. Bonrad, and E. Dörsam, IEEE Trans. Electron Devices **62**, 2871 (2015).
[32] W.J. Scheideler, A. Zeumault, and V. Subramanian, in *2015 73rd Annu. Device Res. Conf. DRC* (2015), pp. 205–206.
[33] G. Grau, J. Cen, H. Kang, R. Kitsomboonloha, W.J. Scheideler, and V. Subramanian, Flex. Print. Electron. **1**, 023002 (2016).
[34] R. Kitsomboonloha, H. Kang, G. Grau, W. Scheideler, and V. Subramanian, Adv. Electron. Mater. **1**, 1500155 (2015).
[35] A. Zeumault, W. Scheideler, G. Grau, J. Smith, and V. Subramanian, Adv. Electron. Mater. **2**, 1500326 (2016).
[36] Y. Li, L. Lan, P. Xiao, S. Sun, Z. Lin, W. Song, E. Song, P. Gao, W. Wu, and J. Peng, ACS Appl. Mater. Interfaces **8**, 19643 (2016).
[37] A. Sneck, H. Ailas, F. Gao, and J. Leppäniemi, ACS Appl. Mater. Interfaces **13**, 41782 (2021).
[38] E. A. Cochran, K. N. Woods, D. W. Johnson, C. J. Page, and S. W. Boettcher, J. Mater. Chem. A **7**, 24124 (2019).
[39] W. Scheideler and V. Subramanian, Nanotechnology **30**, 272001 (2019).
[40] Y.-H. Kim, J.-S. Heo, T.-H. Kim, S. Park, M.-H. Yoon, J. Kim, M.S. Oh, G.-R. Yi, Y.-Y. Noh, and S.K. Park, Nature **489**, 128 (2012).
[41] J. Socratous, K.K. Banger, Y. Vaynzof, A. Sadhanala, A.D. Brown, A. Sepe, U. Steiner, and H. Sirringhaus, Adv. Funct. Mater. **25**, 1873 (2015).
[42] B.-S. Yu, J.-Y. Jeon, B.-C. Kang, W. Lee, Y.-H. Kim, and T.-J. Ha, Sci. Rep. **9**, 8416 (2019).
[43] E. Yarali, C. Koutsiaki, H. Faber, K. Tetzner, E. Yengel, P. Patsalas, N. Kalfagiannis, D.C. Koutsogeorgis, and T.D. Anthopoulos, Adv. Funct. Mater. **30**, 1906022 (2020).
[44] T.-H. Yoo, S.-J. Kwon, H.-S. Kim, J.-M. Hong, J. Ah Lim, and Y.-W. Song, RSC Adv. **4**, 19375 (2014).
[45] T.B. Daunis, K.A. Schroder, and J.W.P. Hsu, Npj Flex. Electron. **4**, 1 (2020).
[46] N.M. Twyman, K. Tetzner, T.D. Anthopoulos, D.J. Payne, and A. Regoutz, Appl. Surf. Sci. **479**, 974 (2019).
[47] H. Huang, H. Hu, J. Zhu, and T. Guo, J. Electron. Mater. **46**, 4497 (2017).
[48] E. Carlos, S. Dellis, N. Kalfagiannis, L. Koutsokeras, D. C. Koutsogeorgis, R. Branquinho, R. Martins, and E. Fortunato, J. Mater. Chem. C **8**, 6176 (2020).
[49] Y. Magari, T. Kataoka, W. Yeh, and M. Furuta, Nat. Commun. **13**, 1078 (2022).

[50] M. Si, Z. Lin, Z. Chen, and P.D. Ye, IEEE Trans. Electron Devices **68**, 6605 (2021).
[51] J. Jia, S. Iwasaki, S. Yamamoto, S. Nakamura, E. Magome, T. Okajima, and Y. Shigesato, ACS Appl. Mater. Interfaces **13**, 31825 (2021).
[52] J.S. Lee, Y.-J. Kwack, and W.-S. Choi, ACS Appl. Mater. Interfaces **5**, 11578 (2013).
[53] A.B. Hamlin, Y. Ye, J.E. Huddy, M.S. Rahman, and W.J. Scheideler, Npj 2D Mater. Appl. **6**, 1 (2022).
[54] Y.-H. Lin, H. Faber, K. Zhao, Q. Wang, A. Amassian, M. McLachlan, and T.D. Anthopoulos, Adv. Mater. **25**, 4340 (2013).
[55] H. Chang, C.-H. Huang, and K. Nomura, ACS Appl. Electron. Mater. **3**, 4943 (2021).
[56] M.T. Hayat, M. Nauman, N. Nazir, S. Ali, and N. Bangash, in *Cadmium Toxic. Toler. Plants*, edited by M. Hasanuzzaman, M.N.V. Prasad, and M. Fujita (Academic Press, 2019), pp. 163–183.
[57] S.T. Meyers, J.T. Anderson, C.M. Hung, J. Thompson, J.F. Wager, and D.A. Keszler, J. Am. Chem. Soc. **130**, 17603 (2008).
[58] K. Liang, H. Ren, D. Li, Y. Wang, Y. Tang, M. Zhao, H. Wang, W. Li, and B. Zhu, J. Mater. Chem. C **9**, 11662 (2021).
[59] K. Liang, R. Wang, B. Huo, H. Ren, D. Li, Y. Wang, Y. Tang, Y. Chen, C. Song, F. Li, B. Ji, H. Wang, and B. Zhu, ACS Nano **16**, 8651 (2022).
[60] S. Jeong, J.-Y. Lee, S. Sook Lee, S.-W. Oh, H. Ho Lee, Y.-H. Seo, B.-H. Ryu, and Y. Choi, J. Mater. Chem. **21**, 17066 (2011).
[61] M. Xie, S. Wu, Z. Chen, Q. Khan, X. Wu, S. Shao, and Z. Cui, RSC Adv. **6**, 41439 (2016).
[62] Y. Wang, X.W. Sun, G.K.L. Goh, H.V. Demir, and H.Y. Yu, IEEE Trans. Electron Devices **58**, 480 (2011).
[63] K. Everaerts, L. Zeng, J.W. Hennek, D.I. Camacho, D. Jariwala, M.J. Bedzyk, M.C. Hersam, and T.J. Marks, ACS Appl. Mater. Interfaces **5**, 11884 (2013).
[64] D.-H. Lee, S.-Y. Han, G. S. Herman, and C. Chang, J. Mater. Chem. **19**, 3135 (2009).
[65] N.N. Mude, R.N. Bukke, J.K. Saha, C. Avis, and J. Jang, Adv. Electron. Mater. **5**, 1900768 (2019).
[66] H. Kim and W.-S. Choi, Ceram. Int. **43**, 4775 (2017).
[67] X. Wang and A. Dodabalapur, Ann. Phys. **530**, 1800341 (2018).
[68] X. Wang and A. Dodabalapur, J. Appl. Phys. **130**, 145302 (2021).
[69] K. Liang, Y. Wang, S. Shao, M. Luo, V. Pecunia, L. Shao, J. Zhao, Z. Chen, L. Mo, and Z. Cui, J. Mater. Chem. C **7**, 6169 (2019).
[70] Y. Zhou and C. Dong, Micromachines **9**, 603 (2018).
[71] C. Lee, W.-Y. Lee, D.W. Kim, H.J. Kim, J.-H. Bae, I.-M. Kang, D. Lim, K. Kim, and J. Jang, Appl. Surf. Sci. **559**, 149971 (2021).
[72] C.R. Allemang and R.L. Peterson, IEEE Electron Device Lett. **40**, 1120 (2019).
[73] S.-Y. Kim, K. Kim, Y. H. Hwang, J. Park, J. Jang, Y. Nam, Y. Kang, M. Kim, H. J. Park, Z. Lee, J. Choi, Y. Kim, S. Jeong, B.-S. Bae, and J.-U. Park, Nanoscale **8**, 17113 (2016).
[74] X. Wei, S. Kumagai, M. Sasaki, S. Watanabe, and J. Takeya, AIP Adv. **11**, 035027 (2021).
[75] Y.-H. Lin, H. Faber, J.G. Labram, E. Stratakis, L. Sygellou, E. Kymakis, N.A. Hastas, R. Li, K. Zhao, A. Amassian, N.D. Treat, M. McLachlan, and T.D. Anthopoulos, Adv. Sci. **2**, 1500058 (2015).
[76] S.-H. Lee, Y.-J. Kwack, J.S. Lee, and W.-S. Choi, ECS Trans. **75**, 127 (2016).
[77] S. Shao, K. Liang, X. Li, J. Zhang, C. Liu, Z. Cui, and J. Zhao, J. Mater. Sci. Technol. **81**, 26 (2021).
[78] E.B. Secor, J. Smith, T.J. Marks, and M.C. Hersam, ACS Appl. Mater. Interfaces **8**, 17428 (2016).
[79] L. Gillan, J. Leppäniemi, K. Eiroma, H. Majumdar, and A. Alastalo, J. Mater. Chem. C **6**, 3220 (2018).

[80] K. Song, D. Kim, X.-S. Li, T. Jun, Y. Jeong, and J. Moon, J. Mater. Chem. **19**, 8881 (2009).
[81] Y. Li, P. He, S. Chen, L. Lan, X. Dai, and J. Peng, ACS Appl. Mater. Interfaces **11**, 28052 (2019).
[82] Y. Tang, C.-H. Huang, and K. Nomura, ACS Nano **16**, 3280 (2022).
[83] A. Zeumault and V. Subramanian, Adv. Funct. Mater. **26**, 955 (2016).
[84] S.A. Singaraju, G.C. Marques, P. Gruber, R. Kruk, H. Hahn, B. Breitung, and J. Aghassi-8 Hagmann, Phys. Status Solidi RRL – Rapid Res. Lett. **14**, 2000252 (2020).
[85] A. Zeumault, S. Ma, and J. Holbery, Phys. Status Solidi A **213**, 2189 (2016).
[86] Z. Wang, X. Zhuang, B. Wang, W. Huang, T.J. Marks, and A. Facchetti, Adv. Funct. Mater. **31**, 2100451 (2021).
[87] D. Sun, C. Chen, J. Zhang, X. Wu, H. Chen, and T. Guo, Appl. Phys. Lett. **112**, 012102 (2018).
[88] M.N. Le, K.-J. Baeg, K.-T. Kim, S.-H. Kang, B.D. Choi, C.-Y. Park, S.-P. Jeon, S. Lee, J.-15 W. Jo, S. Kim, J.-G. Park, D. Ho, J. Hong, M. Kim, H.-K. Kim, C. Kim, K. Kim, Y.-H. Kim, 16 S.K. Park, and M.-G. Kim, Adv. Funct. Mater. **31**, 2103285 (2021).
[89] A. Zavabeti, J.Z. Ou, B.J. Carey, N. Syed, R. Orrell-Trigg, E.L.H. Mayes, C. Xu, O. Kavehei, A.P. O'Mullane, R.B. Kaner, K. Kalantar-zadeh, and T. Daeneke, Science **358**, 332 (2017).
[90] C.-H. Huang, Y. Tang, T.-Y. Yang, Y.-L. Chueh, and K. Nomura, ACS Appl. Mater. Interfaces (2021).
[91] R.S. Datta, N. Syed, A. Zavabeti, A. Jannat, M. Mohiuddin, M. Rokunuzzaman, B. Yue Zhang, M.A. Rahman, P. Atkin, K.A. Messalea, M.B. Ghasemian, E.D. Gaspera, S. Bhattacharyya, M.S. Fuhrer, S.P. Russo, C.F. McConville, D. Esrafilzadeh, K. Kalantar-Zadeh, and T. Daeneke, Nat. Electron. **3**, 51 (2020).
[92] K.A. Messalea, N. Syed, A. Zavabeti, M. Mohiuddin, A. Jannat, P. Aukarasereenont, C.K. Nguyen, M.X. Low, S. Walia, B. Haas, C.T. Koch, N. Mahmood, K. Khoshmanesh, K. Kalantar-Zadeh, and T. Daeneke, ACS Nano **15**, 16067 (2021).
[93] Y. Ye, A.B. Hamlin, J.E. Huddy, M.S. Rahman, and W.J. Scheideler, Adv. Funct. Mater. **n/a**, 2204235 (n.d.).
[94] A. Scholz, L. Zimmermann, U. Gengenbach, L. Koker, Z. Chen, H. Hahn, A. Sikora, M.B. Tahoori, and J. Aghassi-Hagmann, Nat. Commun. **11**, 5543 (2020).
[95] S.-M. Kim, S. Lee, and C.-H. Kim, Org. Electron. **89**, 106034 (2021).
[96] M. Zulqarnain and E. Cantatore, IEEE Open J. Circuits Syst. **2**, 743 (2021).
[97] H. Hu, J. Zhu, M. Chen, T. Guo, and F. Li, Appl. Surf. Sci. **441**, 295 (2018).
[98] T.T. Baby, S.K. Garlapati, S. Dehm, M. Häming, R. Kruk, H. Hahn, and S. Dasgupta, ACS Nano **9**, 3075 (2015).
[99] M. Aman, Y. Takeda, K. Ito, K. Yamamoto, K. Tanaka, H. Matsukizono, W. Nakamura, and N. Makita, J. Soc. Inf. Disp. **29**, 416 (2021).
[100] I. Isakov, A.F. Paterson, O. Solomeshch, N. Tessler, Q. Zhang, J. Li, X. Zhang, Z. Fei, M. Heeney, and T.D. Anthopoulos, Appl. Phys. Lett. **109**, 263301 (2016).
[101] I.Y. Jo, J.-G. Park, J.-H. Moon, J.Y. Jung, D.E. Kim, and K.-J. Baeg, Org. Electron. **75**, 105358 (2019).